

Optimizing the Marangoni effect towards enhanced salt rejection in thermal passive desalination

*Original*

Optimizing the Marangoni effect towards enhanced salt rejection in thermal passive desalination / Stincone, Giovanni; Meo, Roberto Raffaele; Chiavazzo, Eliodoro; Asinari, Pietro; Fasano, Matteo; Morciano, Matteo. - In: DESALINATION. - ISSN 0011-9164. - 583:(2024). [10.1016/j.desal.2024.117673]

*Availability:*

This version is available at: 11583/2988608 since: 2024-05-13T17:03:49Z

*Publisher:*

Elsevier

*Published*

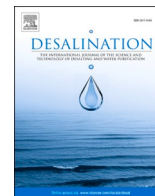
DOI:10.1016/j.desal.2024.117673

*Terms of use:*

This article is made available under terms and conditions as specified in the corresponding bibliographic description in the repository

*Publisher copyright*

(Article begins on next page)



## Optimizing the Marangoni effect towards enhanced salt rejection in thermal passive desalination

Giovanni Stincone<sup>a</sup>, Roberto Raffaele Meo<sup>a</sup>, Eliodoro Chiavazzo<sup>a,b,c</sup>, Pietro Asinari<sup>a,c</sup>, Matteo Fasano<sup>a,b</sup>, Matteo Morciano<sup>a,b,\*</sup>

<sup>a</sup> Department of Energy, Politecnico di Torino, Corso Duca degli Abruzzi 24, 10129 Torino, Italy

<sup>b</sup> Clean Water Center, Politecnico di Torino, Corso Duca degli Abruzzi 24, 10129 Torino, Italy

<sup>c</sup> INRIM, Istituto Nazionale di Ricerca Metrologica, Strada delle Cacce 91, Torino, Italy

### HIGHLIGHTS

- Numerical investigation of Marangoni effect to mitigate salt accumulation
- Marangoni effect leads up to 1000-fold mass transfer increase over diffusive flux.
- Accurate semi-empirical equation for mass transfer vs. Marangoni number is provided.
- Simulated time for passive brine disposal is less than 2 h.

### ARTICLE INFO

#### Keywords:

Marangoni effect  
Passive desalination  
Solar desalination  
Brine discharge  
Water treatment  
Sustainability

### ABSTRACT

Amid escalating water scarcity and rising energy prices, the scientific community strives to propose innovative and efficient water treatment solutions. In this context, solar passive technologies have attracted much attention. Furthermore, recent studies have experimentally revealed that the Marangoni effect, when leveraged in well-designed passive devices, may be a promising pathway towards long-term stable performance. This study presents a comprehensive numerical exploration of applying the Marangoni effect to mitigate salt accumulation, a challenge in long-term system operation. Through an extensive sensitivity analysis, we evaluate the solute molar outflow induced by the Marangoni effect, as different parameters vary. Specifically, the Marangoni effect induces enhanced mass transport, outperforming pure diffusive flow by over three orders of magnitude, under nighttime isothermal conditions. Furthermore, we provide a semi-empirical equation describing accurately the mass transfer versus the Marangoni number. Hence, nighttime brine discharge simulations show rapid salt reduction from the evaporator, reaching seawater-like salinity levels within two hours, setting stage for optimal daytime performance. To the best of our knowledge, this discharge time is the lowest reported in the literature under equivalent conditions. In conclusion we believe that the still poorly explored Marangoni effect may offer a durable mean of providing freshwater, particularly in emergencies.

### 1. Introduction

Water scarcity poses a tremendous global challenge with complex and multidimensional repercussions [1–4]. This pressing problem is fueled by a convergence of interconnected factors, including climate change, population growth and depletion of freshwater resources. As a result, the crisis casts a pervasive shadow over the economic and social landscape of societies worldwide. It is projected that by 2025, nearly two-thirds of the global population will grapple with water scarcity

[1–4]. Moreover, around four billion people currently experience severe water shortages for at least a month annually, with about half a billion people affected year-round [1,3,4]. Cost-effective and sustainable solutions to safeguard future generations' welfare are strongly demanded. In detail, areas like the Middle East, North Africa, and Sub-Saharan Africa, bearing the brunt of severe water stress, often lack the necessary financial resources to adopt expensive grid-connected desalination plants. This underscores the need for advancing technological innovation and implementation strategies towards more cost-effective

\* Corresponding author at: Department of Energy, Politecnico di Torino, Corso Duca degli Abruzzi 24, 10129 Torino, Italy.

E-mail address: [matteo.morciano@polito.it](mailto:matteo.morciano@polito.it) (M. Morciano).

<https://doi.org/10.1016/j.desal.2024.117673>

Received 26 January 2024; Received in revised form 28 March 2024; Accepted 20 April 2024

Available online 26 April 2024

0011-9164/© 2024 The Authors. Published by Elsevier B.V. This is an open access article under the CC BY license (<http://creativecommons.org/licenses/by/4.0/>).

solutions [5–7].

In this context, solar-driven passive desalination techniques, based on interfacial evaporation [8–12], have been recognized as promising due to their versatility, resilience, and efficacy. Lacking moving mechanical parts, these solutions prove particularly effective in emergency scenarios and have come into the scientific spotlight [13,14]. Recent studies focus on the use of advanced nanomaterials [15–20], carbon-based materials [21–24], polymers [25,26], and three-dimensional and/or multistage structures [9,27–31] to increase the solar-to-vapor energy conversion. Moreover, emerging approaches encompass the use of aerogels and tailored cellulose paper or cotton-based water channels to simultaneously optimize fluidic transport and minimize heat dispersion [32–37].

Despite the recent abundant literature on the topic, several critical aspects still remain to make such technology viable [38]. Among those aspects, the challenge of efficient and/or spontaneous brine disposal remains a formidable barrier to the large-scale adoption of passive thermal desalination systems [32,39–41]. Various techniques and strategies have been proposed to tackle this problem. In detail, previous studies have explored the effect of fluid flow engineering techniques to mitigate salt accumulation occurring in the evaporator [42] through guided crystallization and/or controlled salt re-circulation [43]. Guided crystallization induces salt precipitation in specific areas [44,45], while salt re-circulation attempts to prevent such precipitation. Both approaches present challenges, in particular with regard to the implementation of scalable systems able to guarantee long-term stable performance and the manufacturing of materials with particular features [46,47]. Some of the most representative works are briefly discussed here.

Shi and co-workers [48] proposed a three-dimensional solar evaporator that separates the sunlight-absorbing surface from the salt crystallization surface, preventing salt accumulation that could impede evaporation. Concurrently, Ni and co-workers [49], taking a simplified but effective route, developed a floating passive solar distiller with optimized aspect ratio capable of complete salt removal within a few hours. However, both these solutions have limitations concerning scalability and thus distillate productivity. Then, Kashyap and co-workers [50], also focused on the choice of materials, introduced a flexible, anti-fouling structure by customising geometry, pore size and coating. Although efficient, production costs might pose a hurdle in emergency scenarios requiring cost-effective solutions. Others notable studies proposed an hydrogel with anti-clogging features [51], wick-free structures for efficient solar evaporation [42], and device with effective salt rejection driven by thermohaline convection [52]. Notwithstanding these promising and extremely relevant advances, none of these techniques appear to be fully scalable and further efforts are underway.

Recently, innovative studies have revealed the potential role of Marangoni effect in the long-standing salt rejection issue [29,53–56]. These findings might have a profound impact on the future development of such technologies [53]. Theoretical studies supported by experimental evidence have elucidated the underlying mechanism and thus the relationship between the Marangoni effect and the efficient salt rejection. In detail, an advective mechanism may be induced by the presence of a liquid-air interface and by local surface tension gradient enabling significantly superior effective solute transport, i.e., two orders of magnitude higher than traditional diffusion as already reported by Morciano and co-workers [53]. Concurrently, Wu and co-workers [57] proposed a bio-inspired structure (i.e., shaped by 3D-printed cones) with salt rejection capabilities induced by Marangoni-effect driven advective fluid flow. Further developments of this concept were reported by Zou and co-workers, who studied a biomimetic 3D bridge-arch solar evaporator to induce Marangoni flow for long-term salt rejection [43]. Although the exploitation of the Marangoni effect has experimentally proven to be effective in completely removing accumulated salt during daytime operation [43,53], comprehensive theoretical and numerical studies capable of assessing and detailing the influence of the various

parameters determining the performance are yet necessary to gain a thorough understanding and optimally design the systems.

Here, a numerical model based on finite element analysis was developed to further explore advective-diffusive transport phenomena, enhanced by the presence of a liquid-air interface. In detail, the solute transport within the evaporator induced by the surface tension gradient was investigated as a function of operating parameters, such as evaporator geometry and solute concentration. The velocity profiles and the solute outflows were analyzed and discussed in several scenarios. Our work corroborates the effectiveness of the Marangoni effect in removing brine more rapidly, revealing a significantly higher total molar flux leaving the evaporator than that yielded by diffusive processes. Simulations of purely diffusive transport emphasised the significant advantages of the Marangoni effect, exhibiting an increase in the total molar outflow from the evaporator of approximately three orders of magnitude compared to the purely diffusive model.

## 2. Theoretical background and methods

### 2.1. Marangoni effect-driven salt rejection

The sandwich structure sketched in Fig. 1 a) is among the most promising and widely investigated passive desalination system considered in the literature [31,38,53,58]. The sandwich structure consists mainly of a solar absorber, an evaporator, and an air gap through which the water vapor flow passes to reach the condensing layer. The thickness of the air gap is usually optimized according to the boundary conditions and energy sources at disposal to optimize mass transfer permeability coefficient and thermal conductivity (see Fig. 1a). The focus of the research is the investigation of mass transport in the evaporator component, whose features considered are detailed below, of a passive desalination system. The evaporator, accommodating the uniform thin film of aqueous solution (here saltwater) to be thermally treated through interfacial heat localization, is prone to potential salt crystallization phenomena (see Fig. 1a). Indeed, the saltwater in the evaporator is heated up by the incoming thermal energy (e.g., solar energy, absorbed by means of highly selective coating) and a continuous evaporation process takes place, together with concentration of the solute. Then, salt concentration reaches high values in the central region of the evaporator (indicated with dark blue in Fig. 1a), the latter being surrounded by peripheral regions with gradually diminishing concentration (indicated with cornflower blue in Fig. 1a). Such a reduction is due to the presence of the cross sections which are in communication with the seawater basin, through the vertical strips, and arising advective-diffusive phenomena. In detail, the salt concentration gradient induces localized viscous stresses because of the resulting asymmetric interactions experienced by the molecules at the interface. The presence of the liquid-air interface at  $y = \delta_w$  constitutes therefore one of the essential requirements for activating the Marangoni effect. From an engineering perspective, such an interface can be implemented through the use of hydrophilic layers and high porous spacers or as recently proposed by Elimelech and co-workers [59]. In Fig. 1b) a schematic representation of the Marangoni effect-driven salt rejection process occurring in the evaporator is reported. Note that in Fig. 1b), for simplicity of exposition, the liquid-air interface is displayed at the top of the thin film while the support at the bottom (in agreement with the reported Cartesian reference systems).

The state of the art counts a myriad of evaporator structures with special designs and water transportation pathways. Capillary porous wick architectures [14,49,53,60] and rigid and micro-structured capillary layers etched with variously shaped grooves [58,61] are mostly proposed and designed to host the saltwater thin film. However, in order to investigate the potential of the Marangoni effect independently from the particular practical implementation of the evaporator, we will focus on the mass transport in the saltwater thin film disengaging from the intricate details of the evaporator structure, while ensuring a more

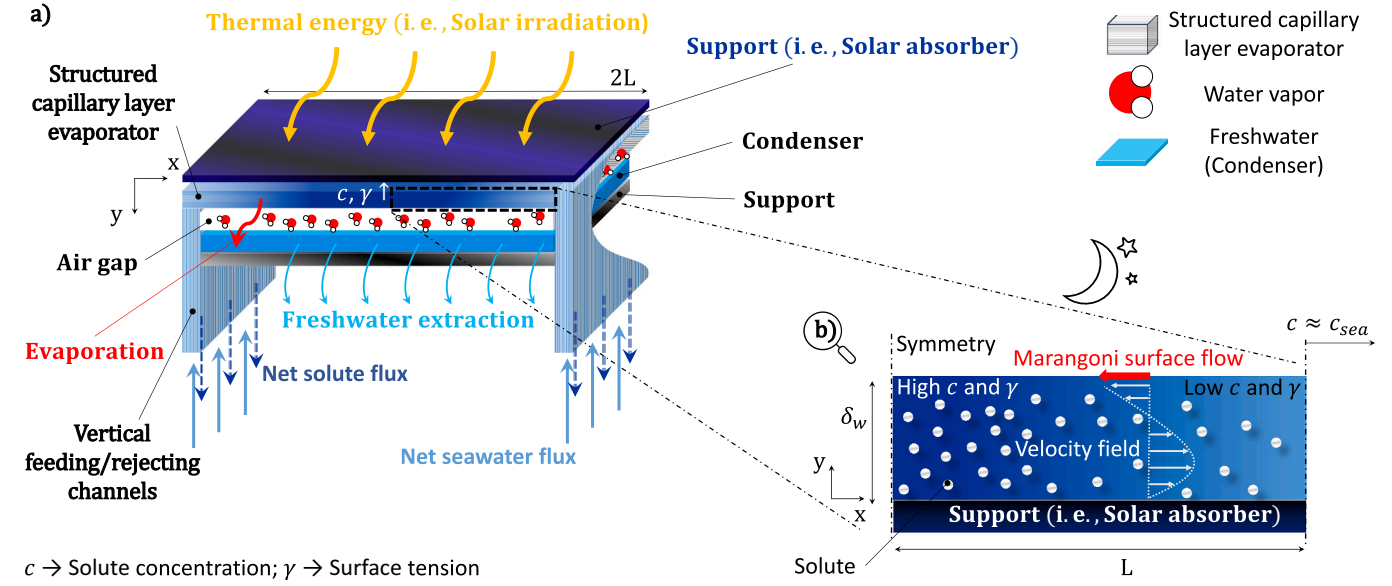


**Fig. 1.** Illustrative picture of the (a) sandwich-like desalination unit, in which the evaporator component is prone to the phenomenon of passive interfacial thermal evaporation, and (b) schematic representation of the Marangoni effect-driven salt rejection process occurring in the evaporator. The vertical extensions immersed in seawater (see panel (a)) allow the supply of seawater (via capillary action, see cornflower blue arrows) and the evacuation of salt (see dark blue arrows). Note that, in panel (b), only half (i.e., the right side) of the horizontal evaporator layer is reported due to symmetry. The portion reported in panel (b) represents the simulation domain. The presence of the liquid-air interface at  $y = \delta_w$  constitutes one of the essential requirements for activating the Marangoni effect. The Marangoni flow at the liquid-air interface arises due to the surface tension (i.e.,  $\gamma$ ) gradient resulting from the gradual reduction in salt concentration (i.e.,  $c$ ) from the left (area most prone to crystallization) to the right boundary (where  $c \approx c_{sea}$ ). Subsequently, the generated velocity field propagates throughout the entire evaporator thickness (i.e.,  $\delta_w$ ). It is important to state that the salt rejection process was investigated under nighttime isothermal conditions.

general study. Thus, the simulation domain (indicated in Fig. 1b) is representative of a saltwater thin film of a specified thickness (i.e.,  $\delta_w$ ) and length (i.e.,  $L$ ). Note that  $L$  (here equal to 1.75 cm [53]) represents only half (i.e., the right side, see Fig. 1a) of the horizontal portion of the whole envisioned evaporator, because of the symmetry. It is worth noting that, to reduce computational costs, the vertical extensions immersed in seawater (see Fig. 1, panel (a)) allowing the supply of seawater and the evacuation of salt were not simulated; rather, appropriate boundary conditions were applied. Therefore, the model can be streamlined by invoking a 2D simulation domain. Indeed, density-driven flow taking place in the vertical feeding/rejecting channels leads to a faster equilibrium process with sea concentration (i.e.,  $c_{sea}$ ).

## 2.2. Numerical simulations of the Marangoni effect

### 2.2.1. Involved physics

COMSOL Multiphysics® simulations were performed to investigate both the purely diffusive and the advective-diffusive (i.e., the Marangoni) phenomenon (see Fig. 1b). Therefore, the volume-averaged Navier–Stokes equations and the transport of diluted species were coupled and solved numerically. Specifically, mass conservation applied to the structured capillary layer evaporator was expressed as:

$$\varepsilon \frac{\partial \rho}{\partial t} + \nabla \cdot (\rho \mathbf{u}) = 0 \quad (1)$$

where  $\rho$  and  $\mathbf{u}$  are the density and the volume-averaged velocity vector of the fluid, respectively,  $\varepsilon$  is the porosity of the structured capillary layer evaporator, which is considered constant in time and spatially homogeneous, and  $t$  the time. Then, the momentum balance equation for fluid flow in the structured capillary layer evaporator was expressed as [62]:

$$\rho \left[ \frac{\partial \mathbf{u}}{\partial t} + \frac{\mathbf{u}}{\varepsilon} \cdot \nabla \mathbf{u} \right] = \nabla \cdot \left[ \mu (\nabla \mathbf{u} + (\nabla \mathbf{u})^T) - \frac{2}{3} \mu (\nabla \cdot \mathbf{u}) \mathbf{I} \right] + \nabla p - \varepsilon \left[ \frac{\mu}{K} + \frac{F_\varepsilon}{\sqrt{K}} \rho |\mathbf{u}| \right] \mathbf{u} \quad (2)$$

where  $K$  and  $F_\varepsilon$  are the permeability and the geometric function of the structured capillary layer evaporator, respectively (see Ref. [62] for further details), which are considered spatially homogeneous. Then,  $p$  is the volume-averaged pressure of fluid,  $\mu$  the dynamic viscosity of the fluid and  $\mathbf{I}$  the identity matrix. In Eq. 2, the gravity term was neglected. The transport of diluted species, which is governed by an advection-diffusion equation, was modelled as:

$$\varepsilon \frac{\partial c_i}{\partial t} + \nabla \cdot \left( -\frac{\varepsilon}{\tau} D_i \nabla c_i \right) + \mathbf{u} \cdot \nabla c_i = R_i \quad (3)$$

where  $c_i$  denotes the mass concentration of the  $i$ -th species (namely, ratio between the mass of solute and the total mass of aqueous solution), and  $D_i$  the molecular isotropic diffusion coefficient of salt in water. Then,  $\tau$  is the tortuosity [53] of the structured capillary layer evaporator.  $R_i$  is the reactive term, which was assumed to be zero based on the premise that the salt remains chemically inert within this context. As extensively discussed in Section 2.1, the porosity  $\varepsilon$  of the structured capillary layer evaporator was considered equal to 1. This assumption will be applied to Eqs. 1, 2 and 3 and consistently maintained henceforth. In this study, the main objective was indeed to explore the potential solute molar flux induced by the Marangoni effect, while diverting attention from the intricate complexity of the myriad of micro-structured capillary layers with high porosity (i.e.,  $> 0.9$ , as reported in Refs. [9, 53]), which accommodate the simulated volume of saltwater. The density  $\rho$  and the dynamic viscosity  $\mu$  of the fluid are solute concentration-dependent properties, evaluated through empirical correlations [63]. In detail, the expression for density was evaluated as follows:

$$\rho = \rho_0 (1 + \beta c) \quad (4)$$

where  $\rho_0$  represents the density of freshwater at ambient temperature (i.e., equal to  $0.9982 \text{ kg L}^{-1}$ ), and  $\beta$  is a fitting parameter (R-square  $\approx 0.99$ ) derived from the linear regression curve outlining the density trend as a function of concentration [64]. For sodium chloride-based aqueous solution  $\beta$  is equal to  $6.46 \cdot 10^{-4} \text{ L g}^{-1}$ . The expression for dynamic viscosity was given by:

$$\mu = \frac{\mu_0}{1 - \delta c} \quad (5)$$

where  $\mu_0$  is the dynamic viscosity of pure water and has a value of  $0.001 \text{ kg m}^{-1} \text{ s}^{-1}$ , while  $\delta$  is a fitting parameter (R-square  $\approx 0.99$ ) derived from the linear regression curve outlining the viscosity trend as a function of concentration [64]. For sodium chloride-based aqueous solution  $\delta$  is equal to  $1.566 \cdot 10^{-4} \text{ L g}^{-1}$ .

Finally, the total outgoing solute molar fluxes in the case when the Marangoni effect is active and in the case of pure diffusion only were evaluated by the following equations, respectively [53]:

$$N_{\text{Marangoni}} = \int_0^{\delta_w} (-D_i \nabla c_i + \mathbf{u} c_i) \cdot \mathbf{n} \, dy \quad (6)$$

$$N_{\text{Diffusive}} = \int_0^{\delta_w} (-D_i \nabla c_i) \cdot \mathbf{n} \, dy \quad (7)$$

where  $\mathbf{n}$  represents the unit normal vector. Note that  $\mathbf{u}$  appearing in Eq. 6 accounts for advective flow motion generated by the surface tension gradient at the interface, which does not occur in purely diffusive flow motion (see Eq. 7). The comparison of the effectiveness of transport mechanisms due to the Marangoni effect and that of pure molecular diffusion was accomplished by evaluating the ratio of the corresponding stationary molar fluxes at the outlet section, as follows [53]:

$$R = \frac{N_{\text{Marangoni}}}{N_{\text{Diffusive}}} = \frac{\int_0^{\delta_w} (-D_i \nabla c_i + \mathbf{u} c_i) \cdot \mathbf{n} \, dy}{\int_0^{\delta_w} (-D_i \nabla c_i) \cdot \mathbf{n} \, dy} \quad (8)$$

It is worth pointing out that, henceforth, we considered sodium chloride as the only species present in water. Thus, a value of  $1.5 \cdot 10^{-9} \text{ m}^2 \text{ s}^{-1}$  [53,65] was assigned to  $D_i$ . Finally, it is worth mentioning that in this study, the Marangoni effect is exclusively induced by concentration gradients. Specifically, our simulations aimed to investigate the ability of the evaporator to re-establish the initial seawater concentration during the nighttime hours from high levels of salt concentration throughout the domain, under isothermal conditions.

### 2.2.2. Initial and boundary conditions

A Dirichlet condition was applied to the left boundary of the control volume (i.e.,  $x = 0$  and  $\forall y$ , see Fig. 1b) to fix the maximum concentration value (i.e.,  $c_{\text{max}}$ ). The  $c_{\text{max}}$  value, determining the driving force of the process, was varied from 700 to  $3400 \text{ mol m}^{-3}$  (namely up to  $200 \text{ g L}^{-1}$ , being the molecular weight of sodium chloride equal to  $58.5 \text{ g mol}^{-1}$ , which is typical value of brine [42,53]). These values were intended to mimic different scenarios and thus varying levels of salt accumulation on the evaporator layer, which depend on the evaporation rate and thus the intensity of solar radiation or thermal energy absorbed during daily operation. As an example, considering a typical thermal efficiency of around 75 % for the interfacial passive thermal evaporation process, consistent with experimental findings reported in the comprehensive review paper published by Tao and co-workers [10], along with a solar irradiation of  $1000 \text{ W m}^{-2}$  and  $\delta_w$  equal to 1 mm, a concentration of  $200 \text{ g L}^{-1}$  would be attained within approximately 1.5 h of operation. Whilst, when considering  $\delta_w$  equal to 5 mm, achieving the same concentration of  $200 \text{ g L}^{-1}$  would require approximately 8 h of operation. These time-dependent concentration values were estimated using the analytical approach detailed in Ref. [66]. On the other hand, the open boundary condition was applied to the right

boundary of the control volume (i.e.,  $x = 0$  and  $\forall y$ , see Fig. 1b), namely:

$$\begin{cases} -\mathbf{n} \cdot (-D \nabla c) = 0 & \text{if } \mathbf{u} \cdot \mathbf{n} \geq 0 \\ c = c_{\text{sea}} & \text{if } \mathbf{u} \cdot \mathbf{n} < 0 \end{cases} \quad (9)$$

This condition ensures that when the velocity vector  $\mathbf{u}$  is directed outwards, there is no diffusive mass transfer normal to the boundary. However, when the velocity vector  $\mathbf{u}$  is directed inwards, the concentration  $c$  is set to a fixed value, namely the concentration of the seawater  $c_{\text{sea}}$ , which is equal to  $600 \text{ mol m}^{-3}$  (i.e.,  $35 \text{ g L}^{-1}$ ). Moreover, a step function was used to define the initial volume concentration profile in the evaporator and thus smooth the transition from  $c_{x=0}$  to  $c_{x=L}$ . This approach is useful to prevent potential convergence issues of the simulation in the first time steps due to steep gradients. Then, no normal mass fluxes were considered through the upper and lower boundaries (i.e.,  $y = \delta_w$  and  $y = 0$ , respectively and  $\forall x$ , see Fig. 1b), which are therefore impermeable:

$$-\mathbf{n} \cdot \rho \mathbf{u} = 0 \quad (10)$$

$$-\mathbf{n} \cdot (-D \nabla c) = 0 \quad (11)$$

The Marangoni effect was included into the model through a slip condition applied to the upper boundary (i.e.,  $y = \delta_w$  and  $\forall x$ , see Fig. 1b). This boundary condition is key to reproduce the velocity at the liquid–air interface under the existence of surface tension gradient, and can be articulated, in case of  $\varepsilon = 1$ , as follows:

$$\left[ -\rho \mathbf{I} + \mu (\nabla \mathbf{u} + (\nabla \mathbf{u})^T) - \frac{2}{3} \mu (\nabla \cdot \mathbf{u}) \mathbf{I} \right] \cdot \mathbf{n} = \sigma \nabla c \quad (12)$$

where  $\sigma$  stands for the derivative of the surface tension  $\gamma$  with respect to the concentration, denoted as  $\sigma = \frac{\partial \gamma}{\partial c}$ . Here,  $\sigma$  was equal to  $1.76 \cdot 10^{-6} \frac{\text{N m}^{-1}}{\text{mol m}^{-3}}$  [53]. Clearly, when studying the purely diffusive mass transport, the slip boundary condition was removed from the model. Instead, no slip boundary condition was applied to the lower boundary (i.e.,  $y = 0$  and  $\forall x$ , see Fig. 1b), because of the contact of the fluid with a not moving wall, namely the support.

The presence of high concentration gradients within the solution sometimes increased the susceptibility to numerical errors, primarily due to the dominant advective transport phenomena. Consequently, attention was given to optimize the model setup, particularly by fine-tuning solver parameters such as the relative error tolerance, which ranged between  $10^{-2}$  and  $10^{-3}$ .

Moreover, to ensure consistent and reliable results across different levels of mesh refinement, a mesh independence study was conducted. The convergence criterion established involved systematically varying the mesh size and assessing the impact on the simulation results. In detail, it requires that the outgoing solute molar flux trend tends to a plateau in the convergence plot, which suggests that additional refinement does not significantly affect the results. In all cases the outgoing solute molar flux variation remained consistently below 15 % against a mesh element number variation of at least 35 %, depending on the specific case under consideration. It is worth noting that 15 % represents the maximum accepted deviation, which was encountered in a mere 10 % of simulated cases.

### 2.3. Salt discharge during nighttime

For the sake of completeness, additional simulation was performed to investigate a complete discharge process and the related time needed. In detail, the simulation aimed to further explore the ability of the evaporator to restore, during the nighttime, the initial salt concentration of the sea starting from higher values over the entire domain. In this way, long-term stable performance can be ensured. The simulation was based on the same physical models described in the previous section. Adjustments were then introduced to remove the Dirichlet condition previously applied to the left boundary (i.e.,  $c_{x=0} = c_{\text{max}}$ ), which



imposed a constant concentration gradient during the simulation. Then, a uniform initial concentration profile was introduced throughout the domain (i.e.,  $c(x, y, t = 0) = c_{max} = 200 \text{ g L}^{-1}$ ) to replicate the most challenging salt removal scenario after daily operation of the desalination system. The transient study was conducted for a duration of 6 h. The aim of the simulation is to provide valuable insights into the dynamics of salt rejection process (e.g., during nighttime) and to offer a comprehensive understanding of the ability of the evaporator to recover and maintain optimal performance, even under challenging operational conditions. It is worth mentioning that the transient model was previously employed and validated experimentally in Ref. [53].

### 3. Results and discussions

#### 3.1. Optimizing the Marangoni effect

First, a study was performed to quantify the impact of the concentration gradient on mass transport within the saltwater thin film. To this purpose, the velocity fields and the resulting outgoing solute molar flows induced by the Marangoni effect were thoroughly analyzed and discussed (see Fig. 2). The concentration gradient throughout the evaporator, and consequently the surface tension gradient that is established at the liquid-air interface (i.e., at  $y = \delta_w$ ), was fine-tuned and imposed by maintaining a constant concentration value at the section communicating with the sea (i.e.,  $c_{x=L} = 600 \text{ mol m}^{-3}$ ) and varying the concentration value at  $x = 0$ , where the concentration is expected to reach its maximum value at the end of the daily operating cycle.

Results reported in Fig. 2 refer to  $\delta_w$  equal to 1 mm. In detail, the steady-state velocity profiles generated along the  $y$  direction and at  $x = L$  are shown in Fig. 2a) for various concentration gradients. Here,  $c_{x=0}$  was varied from 700 to 3400  $\text{mol m}^{-3}$ . The resulting pressure difference at the liquid-air interface ranged from approximately 0.01 Pa to 0.28 Pa, being  $\sigma$  equal to  $1.76 \cdot 10^{-6} \frac{\text{N m}^{-1}}{\text{mol m}^{-3}}$ . At higher  $c_{x=0}$  values, the surface tension gradient at the liquid-air interface increases, affecting the fluid shear flow and leading to enhanced advective motion throughout the saltwater layer. As a result, enhanced salt evacuation from the control volume occurs.

The observed reverse flow was the result of the slip condition at the liquid-air interface (i.e., at  $y = \delta_w$ ) and the no-slip condition applied to the lower boundary (i.e.,  $y = 0$ ). In detail, the velocity field assumed negative values in the upper part of the control volume, bounded by a  $y$ -value equal to  $\approx \frac{2}{3} \delta_w$  and the interface. Indeed, at the interface, par-

ticles are transported from the lower to the higher concentration region due to tangential viscous actions. This process establishes internal recirculation, allowing effective dilution of the higher concentration phase. Furthermore, results demonstrate that with an increasing concentration gradient, a gradual augmentation in the magnitude of both positive and negative velocity components is observed.

The salt rejection capacity, as quantified by the net outgoing solute molar flux, is closely related to the direction and magnitude of velocity components developed in the domain. In detail, as the concentration gradient increases, the net outgoing solute molar flux increases. In Fig. 2b), the corresponding net molar fluxes (driven by the Marangoni effect and evaluated by Eq. 6) were reported as a function of time. These outgoing fluxes were calculated at the section communicating with the sea (i.e., at  $x = L$ , see Fig. 1), which acts as the outlet section for the salt ions. After a short transient period, the molar fluxes reached a steady-state condition in all scenarios.

We then extended this study to different values of  $\delta_w$ . Indeed, understanding how the thickness of the saltwater film may affect salt rejection process, and thus the mass transport within the control volume, becomes paramount to proceed with optimization of the device design. To this purpose, sensitivity analyses of the velocity profiles and the corresponding molar fluxes were performed varying  $\delta_w$  from 0.5 to 5 mm. The choice of such values for solar and passive systems lies in manufacturing considerations. Evaporators with a thickness of less than 0.5 mm would be difficult to manufacture and manage; on the other hand, a thickness higher than 5 mm would result in a reduced localization of thermal energy [8] (e.g. solar energy) and higher heat capacity. Results were summarized in Fig. 3.

In detail, Fig. 3a) showcases the influence of  $\delta_w$  on the steady-state velocity profiles, in case of wall at  $x = 0$ . Here,  $c_{x=0}$  was set equal to 1000  $\text{mol m}^{-3}$  as an exemplificative case study. From the reported trend, it may be inferred that increasing  $\delta_w$  causes a reduction in the magnitude of the maximum velocities in the  $x$  – direction along the  $y$  – axis. This is due to a re-mixing of the moving water layer at the surface into a larger volume as thickness increases, and thus fulfilling continuity equation. Therefore, the benefit of increasing the evaporator thickness due to the larger solute discharge cross-section was mitigated by generating a flatter flow field. Furthermore, it is essential to emphasize that the reverse flow induced by the Marangoni effect invariably arose at  $y \approx \frac{2}{3} \delta_w$ , with a discrepancy of 6 % at most. This condition may be demonstrated through a simplified analytical formulation based on the assumption that  $u_x \frac{\partial u_x}{\partial x}$  is much smaller than  $\frac{\mu}{\rho} \frac{\partial^2 u_x}{\partial y^2}$  (i.e.,  $\frac{\Delta y}{L} \ll \frac{4\mu^2 L}{\rho \delta_w^3}$ ) and

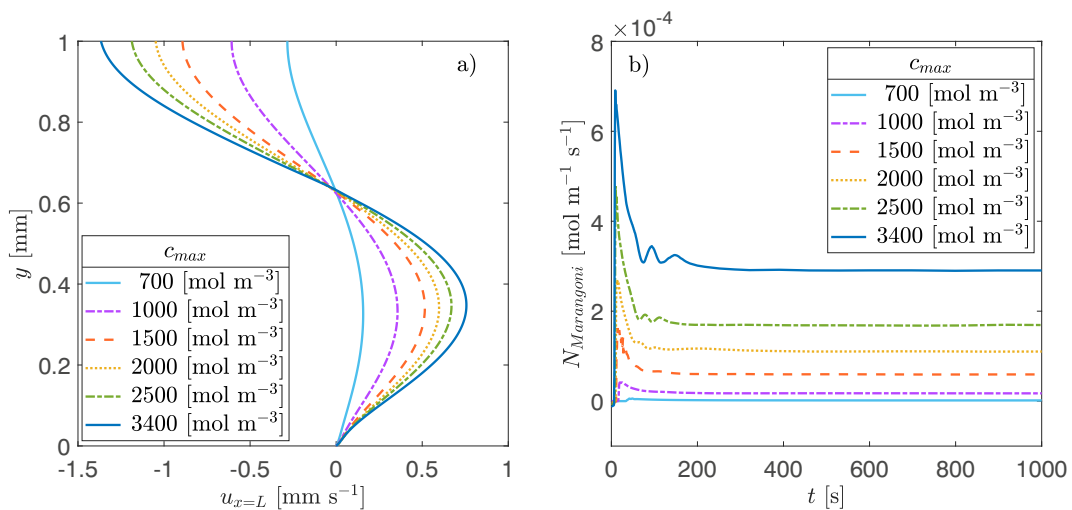
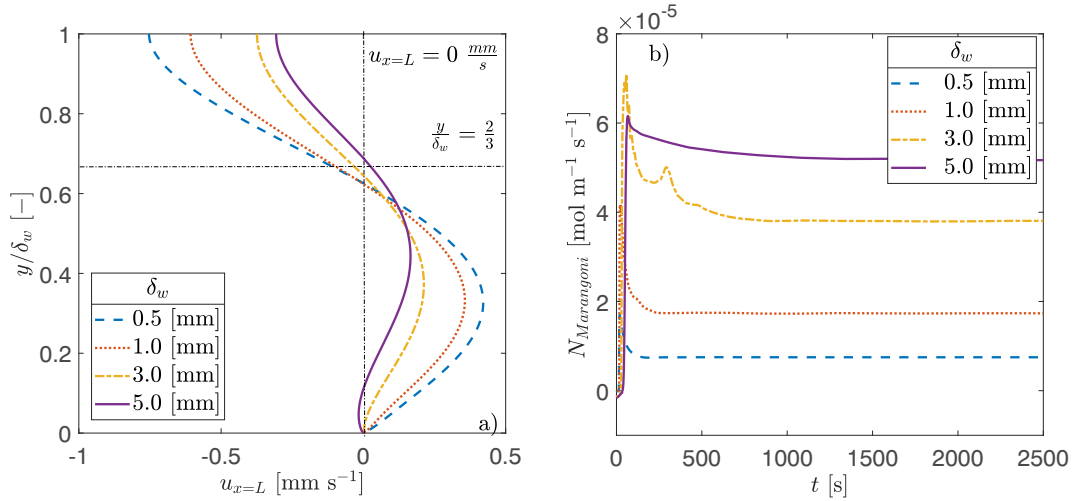


Fig. 2. Salt rejection performance under varying concentration gradient (i.e.,  $\frac{c_{x=0}-c_{x=L}}{L}$ ). (a) Steady-state velocity profiles and (b) time-dependent net outgoing Marangoni-driven solute molar flux, evaluated at  $x = L$ . The results were achieved by varying the value of the salt concentration at  $x = 0$ , from 700 and 3400  $\text{mol m}^{-3}$ , and considering  $c_{x=L}$  constant and equal to  $c_{sea}$  (i.e., 600  $\text{mol m}^{-3}$  or 35  $\text{g L}^{-1}$ ). The results refer to  $\delta_w$  equal to 1 mm.



**Fig. 3.** Salt rejection performance under varying  $\delta_w$  values. (a) Steady-state velocity profiles and (b) time-dependent net outgoing Marangoni-driven solute molar flux, evaluated at  $x = L$ . The results were achieved by varying the  $\delta_w$  value from 0.5 and 5 mm. The results refer to  $c_{x=0}$  equal to 1000 mol m<sup>-3</sup>.

imposing equal to zero the average velocity over the saltwater thin film cross-section (i.e., imposing the continuity equation). The streamlined analytical formulation implies indeed the following parabolic velocity profile  $u_x = y \frac{\partial \gamma}{\partial x} \frac{1}{2\mu} \left( \frac{3y}{2\delta_w} - 1 \right)$ , as reported in Ref. [53]. Interestingly, for  $\delta_w$  values higher than 3 mm, see purple line in Fig. 3a, negative velocity values may also be observed at the outlet cross-section even approaching the boundary where the no-slip condition was applied. This may be due to the reduced velocity in the  $x$ -direction at the outlet section. In Fig. 3b), the corresponding net molar fluxes driven by the Marangoni effect and evaluated by Eq. 6 were reported as a function of time. Disregarding the short transient phase, which may sometimes exhibit unavoidable numerical instabilities, the focus was turned to the dependence of the steady-state molar outflow on the thickness and imposed concentration gradient. In the Fig. 4, the steady-state net molar fluxes driven by the Marangoni effect as a function of  $\delta_w$  were plotted under varying concentration difference (i.e.,  $\Delta c = c_{x=0} - c_{x=L}$ ). Considering the case study analyzed in Fig. 3 (i.e.,  $c_{x=0}$  equal to 1000 mol m<sup>-3</sup>), the results (see blue circles in Fig. 4) illustrated a potential 590 % increase in total molar outflow by varying  $\delta_w$  from 0.5 mm

to 5 mm. However, Fig. 4 clearly reveals the asymptotic behaviour of the thickness-dependent  $N_{Marangoni}$  owing to the flatter flow field yielded by the increase in  $\delta_w$ . Moreover, as  $\Delta c$  increases (see lighter blue curves), the relative  $N_{Marangoni}$  increases due to  $\delta_w$  drops. In particular, a potential 350 % increase in total molar outflow was observed for  $\Delta c$  equal to 2800 mol m<sup>-3</sup>, by varying  $\delta_w$  from 0.5 mm to 5 mm.

For completeness and for clearer insights at local level, the surface plots related to the steady-state concentration distribution in the control volume were reported in Fig. 5, for different  $\delta_w$  values. The knowledge of the concentration value reached locally in the device is crucial to carry out a geometry design process that rules out possible stagnation zones and thus assess whether or not the device may be partially affected by drops in productivity during the day. Indeed, the evaporation rate strongly depends on the local value of solute concentration present in the aqueous solution.

Determining the optimal setup may be accomplished by examining both the absolute and relative capacities of the Marangoni effect, comparing it, e.g., with a purely diffusive transport case where no liquid-air interface is available. Therefore, with the aim of emphasizing the

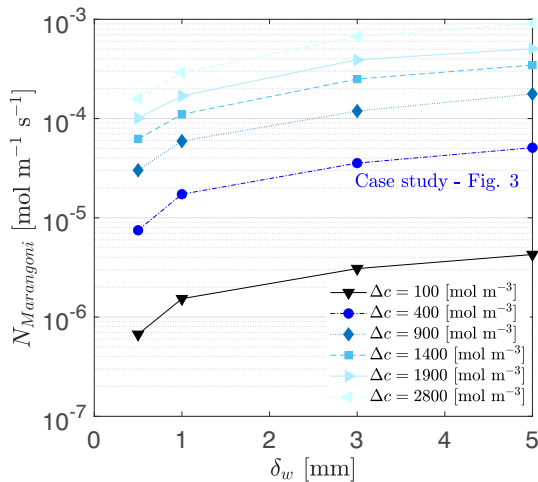


**Fig. 4.** Steady-state net molar fluxes driven by the Marangoni effect as a function of  $\delta_w$  were plotted under varying concentration difference (i.e.,  $\Delta c = c_{x=0} - c_{x=L}$ ). Four different  $\delta_w$  values were considered, i.e., 0.5, 1, 3 and 5 mm. Moreover, the  $c_{max}$  value, determining the driving force of the process, was varied from 700 to 3400 mol m<sup>-3</sup>.

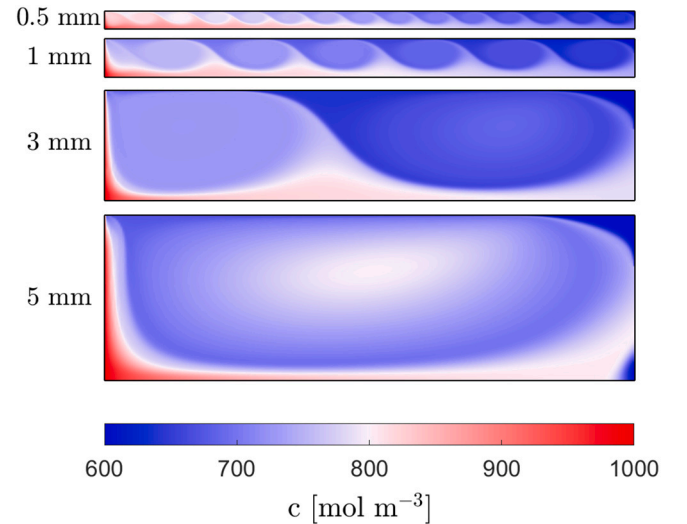


**Fig. 5.** Steady-state concentration surface plots, including the Marangoni effect. The results refer to  $c_{x=0}$  equal to 1000 mol m<sup>-3</sup> and  $c_{x=L}$  equal to  $c_{sea}$ . Four different  $\delta_w$  values were considered, i.e., 0.5, 1, 3 and 5 mm; whilst  $L$  is constant and equal to 1.75 cm.

possible advantage provided by the Marangoni effect compared to the simple case of pure diffusion, the latter was also simulated and the results compared. Specifically, in Fig. 6, the steady-state net outgoing molar flux in case of a) Marangoni effect and b) classical molecular diffusion (where  $D$  is equal to  $1.5 \times 10^{-9} \text{ m}^2 \text{ s}^{-1}$  [65]) were reported as a function of the concentration difference (i.e.,  $\Delta c = c_{x=0} - c_{x=L}$ ). To simultaneously highlight the differences due to the simulation domain dimensions, the calculations were performed for each  $\delta_w$  value proposed in this work.

In the case of purely diffusive regimes (see Fig. 6b), the molar flux under steady-state conditions obviously exhibits a linear dependence on the concentration gradient and the thickness of the domain. In contrast, the molar flux determined by the Marangoni effect (see Fig. 6a) exhibits a trend with an increasing steepness moving from lower to higher concentration gradients. Furthermore, the potential for increasing the absolute salt rejection capacity by using a larger evacuation surface area (i.e.,  $\delta_w$ ) is evident with all concentration gradients analyzed. Then, in Fig. 7a the ratio between the outgoing molar fluxes  $R$  (see Eq. 8) was analyzed and reported as a function of the driving force.

The presence of a surface tension gradient adds a preponderant contribution to mass transport, compared with the case of purely diffusive transport. This effect becomes increasingly significant as the concentration gradient increases. However, it is worth observing that  $R$  exhibits an asymptotic trend with respect to the driving force. This phenomenon can be explained by considering the significant influence of the fluid's viscosity on advective motion. In the presence of sharp saline gradients, the resistance imposed by viscosity increases with a non-linear behaviour, constraining the fluid's response to tension gradients associated with the Marangoni effect. Thus, even as the driving force increases with higher concentration differences, the viscous effect prevents a proportional rise in the advective salt flux, leading to an asymptotic trend. On the other hand, in the context of diffusive transport, the flux increases linearly with the concentration gradient and remains unaffected by the fluid's viscosity. Another key insight is characterized by the fact that this saturation propensity is more pronounced in the case of higher thicknesses. This is due to higher velocity values (see Fig. 3a) established with lower  $\delta_w$ . As a result, for larger thicknesses, the Marangoni effect will progressively exert less influence on the increase in molar flux prompted by the increase in the concentration gradient. As evident in Fig. 7a, the total molar flux obtained in the presence of the Marangoni effect may reach values generally 2 orders of magnitude higher than the purely diffusive one. For thicknesses of less than 1 mm, even 3 orders of magnitude differences were reached.

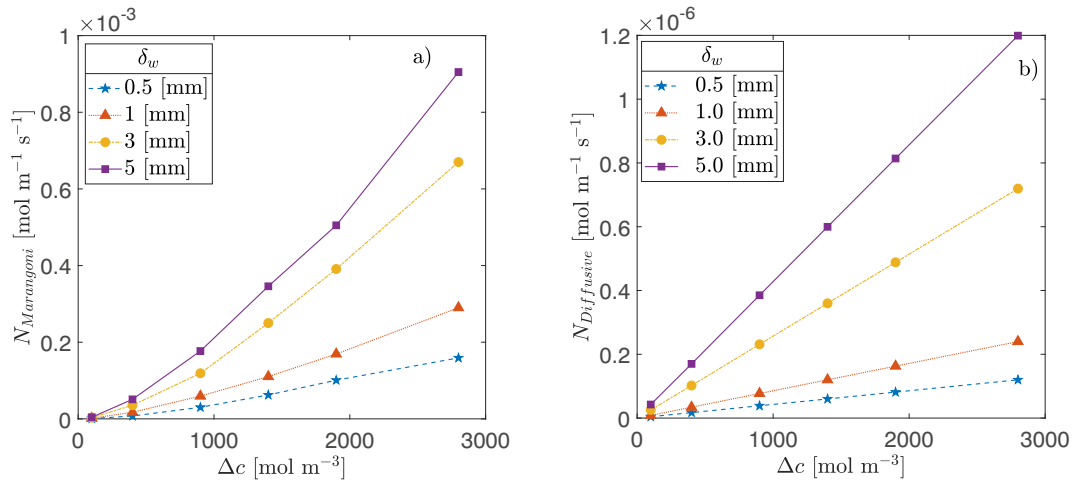


**Fig. 6.** Steady-state net outgoing molar flux in case of a) Marangoni effect and of b) classical molecular diffusion, under varying concentration difference (i.e.,  $\Delta c = c_{x=0} - c_{x=L}$ ). Four  $\delta_w$  values were considered. Results refer to Eqs. 6 and 7, respectively. In case of purely diffusive flow, the slip boundary condition at the upper boundary was replaced with a no-slip condition. Moreover, the simulation time of the diffusive flow was augmented up to  $t = 40 \text{ h}$  to ensure steady-state conditions for all simulated cases.

From an engineering perspective, exploring the outgoing molar flux augmentation trend as a function of the dimensionless driving force would be interesting and helpful. In order to eventually generalise the phenomenon under investigation, the results presented in Fig. 7a were thus adimensionalised and regrouped in Fig. 7b. To this purpose, the well-known Marangoni number (i.e.,  $Ma = \frac{\sigma \Delta c \delta_w}{D \mu}$ ), the parameter  $R$  (defined by Eq. 8) and the layer thickness (i.e.,  $\delta_w$ ) normalised with respect to the length  $L$  were introduced. Interestingly, the trend describing the outgoing molar flux enhancement due to the Marangoni effect as a function of the driving force can be well fitted (R-square = 0.977) by a semi-empirical, unique and simple equation, namely  $R \left(\frac{\delta_w}{L}\right)^a = b Ma^c$ . In detail, the y-axis of Fig. 7b shows the values of  $R$  scaled by  $\left(\frac{\delta_w}{L}\right)^a$ , being  $a = 5.156 \times 10^{-2}$  a fitting parameter. This scaling is employed to account for the varying volume and hence viscous stresses involved while simulating different  $\delta_w$ , and thus to re-scale the  $R$  increase as  $Ma$  increases. While the x-axis shows  $Ma$  elevated to the fitting parameter  $c = 7.685 \times 10^{-1}$ , the whole multiplied by a fitting parameter  $b = 5.254 \times 10^{-1}$ . Similar correlations involving Marangoni number and induced convective mass transfer are reported in the literature [67]. The symbols represented in Fig. 7b refer to all the configurations tested in this paper.

### 3.2. Simulated salt discharge during nighttime

Finally, in Fig. 8a, the time-dependent salt concentration within the layer was reported. The aim was to investigate a complete discharge process and the related time needed, testing the ability of the evaporator to restore the initial salt concentration of the sea during the nighttime. The concentration values were obtained as an average over the control volume. Specifically,  $\delta_w$  was assumed to be equal to 5 mm, thus considering a more design-friendly geometry as well as the case where higher  $N_{\text{Marangoni}}$  occurs.

Starting from a concentration value equal to  $3400 \text{ mol m}^{-3}$  (i.e.,  $200 \text{ g L}^{-1}$ , which is typical value of brine) over the entire control volume, the concentration of the aqueous solution rapidly decreases within the first 30 min. Subsequently, the considerable reduction in the concentration gradient led to a dampening effect on the salt evacuation rate, in any case reaching a concentration of  $600 \text{ mol m}^{-3}$  (i.e.,  $c_{\text{sea}}$ ) in less than 2 h. Therefore, the device would be able to passively reject 100 % of salt accumulated during daytime operations and reach equilibrium with seawater well within the nighttime. The solution investigated in



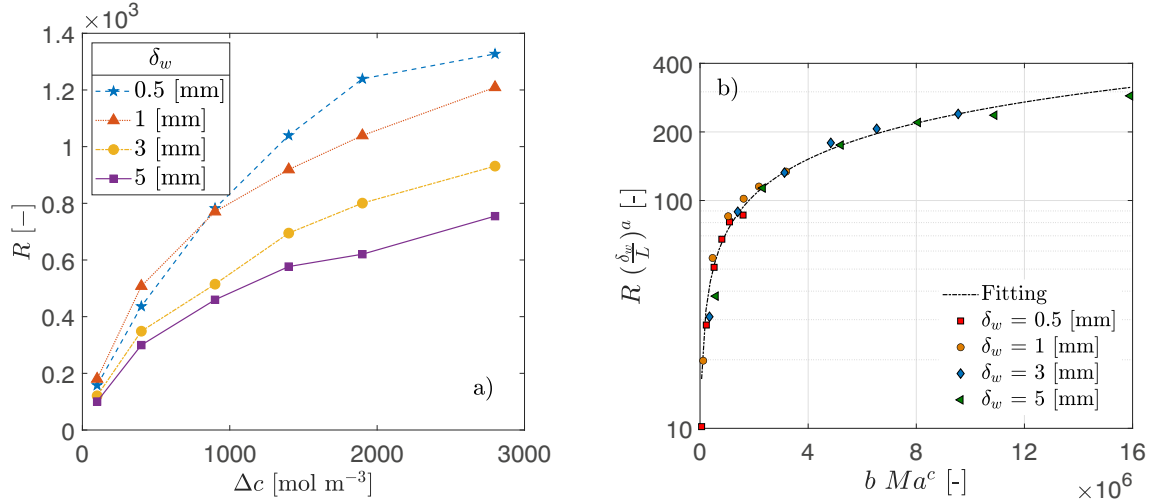


**Fig. 7.** a) Ratio between the steady-state outgoing molar flux in case of Marangoni effect and purely molecular diffusion (defined by Eq. 8), under varying concentration difference (i.e.,  $\Delta c = c_{x=0} - c_{x=L}$ ). Different domain thicknesses are shown. b) Relationship between the ratio  $R$  between the steady-state outgoing molar flux in case of Marangoni effect and purely molecular diffusion (defined by Eq. 8) and the Marangoni number (i.e.,  $Ma$ ). Symbols refer to all configurations tested in this paper. The resulting trend can be well fitted (R-square = 0.977) by the power function  $R \left(\frac{\delta_w}{L}\right)^a = b Ma^c$  (dot-dashed black line), being  $a = 5.156 \times 10^{-2}$ ,  $b = 5.254 \times 10^{-1}$ ,  $c = 7.685 \times 10^{-1}$  the fitting parameters. Note that the y-axis is on a logarithmic scale.

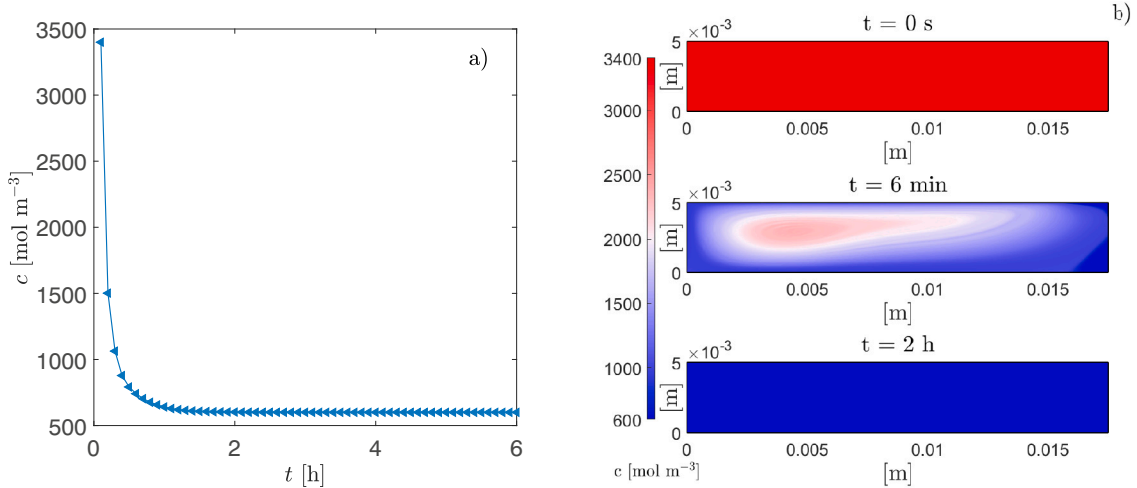


**Fig. 8.** Simulated salt discharge from the evaporator during nighttime. a) Time evolution of the average salt concentration over the entire control volume and b) transient concentration surface plots, in case of  $\delta_w$  equal to 5 mm. The initial salt concentration over the entire domain was set to 3400  $\text{mol m}^{-3}$ .

this study therefore turned out to be highly promising towards real applications. Indeed, a faster discharge process may result in faster production of fresh water, making the technology more practical for dealing with water shortages and emergency situations. It is worth mentioning that, in our previous study [53], a 75 % concentration decrease was observed after 2 h; whilst, the device was able to passively reject 100 % of the salt accumulated during the daytime operations after  $\approx 4$  h. This suggests yet again the importance of carrying out optimization studies of the poorly explored Marangoni effect.

To conclude, the proposed model allows for a local and accurate assessment of salt rejection times, and thus provides a time- and space-dependent assessment of solute concentration (i.e.,  $c(x,t)$ ). This is extremely useful at the design stage. At the same time, conducting experimental studies to measure the salinity of water in such a devices (e.g., steam generators, interfacial evaporators, and desalination devices) during their operation posed more than significant challenges. To date, most of the experimental work on this topic, although offering a significant contribution to this area, was performed with non-

quantitative and/or destructive techniques, which have limitations. In this regard, the research works discussed in the introduction, demonstrating the potential of the Marangoni effect to induce enhanced recirculation of brine or guided crystallization of salt, were summarized in Table 1, for the sake of compactness. As detailed, Refs. [29, 54–57] rely on indirect method to evaluate the solute concentration, where the dynamics of salt distribution/accumulation inside the evaporator and diffusion processes were studied only by image analysis. In detail, the concentration and any salt crystallization on photothermal surfaces was monitored using digital photos. This demonstrates the importance to analyze systematically, theoretically and numerically, solute transport as a function of time.

#### 4. Conclusions

Our research optimizes the potential of the Marangoni effect in generating enhanced mass transport, thus providing a highly effective solution to the salt accumulation issue. Continuum fluid dynamics

**Table 1**

Recent research papers demonstrating the potential of the Marangoni effect to induce enhanced re-circulation of brine or guided crystallization of salt. Materials used, concentration evaluation method (indicated by CEM), the type of research (i.e., experimental and/or numerical research), and year of publication were indicated.  $c(x, t)$  refers to time- and space-dependent solute concentration. PS/LC stands for polystyrene/lignocellulose.

Salt rejection strategy	Material	CEM	Research	Ref.
Enhanced re-circulation	Low-cost wick	Direct [ $c(x, t)$ ]	Exp./ Num.	2020 [53]
Guided crystallization	3D printed nanocomposite	Indirect	Exp.	2020 [57]
Enhanced re-circulation	Coated hydrophilic PS/LC skeleton	Indirect	Exp.	2021 [56]
Enhanced re-circulation	Composite resin	Direct [ $c(x)$ ]	Exp./ Num.	2021 [43]
Guided crystallization	Fabric decorated with MXene	Indirect	Exp.	2022 [29]
Guided crystallization	Wood shell and hydrogel	Indirect	Exp./ Num.	2023 [54]
Enhanced re-circulation	Coated copper mesh	Indirect	Exp./ Num.	2023 [55]
Enhanced re-circulation	Low-cost wick	Direct [ $c(x, t)$ ]	Num.	This work

simulations were performed. In detail, the Navier–Stokes equations and the transport of diluted species were coupled and solved numerically to investigate the advection–diffusion phenomenon in presence of a liquid–air interface. A detailed analysis of the characteristics of the velocity field driven by the surface tension gradient and the advective–diffusive flow of species was performed to identify the key parameters that influence the transport mechanisms. Sensitivity analyses have elucidated the influences of salt concentration gradient and evaporator thickness on salt transport capacities. In the case presented, it was found that the molar flux associated with advective–diffusive phenomena is directly proportional to the thickness of the evaporation layer and the concentration gradient in the solution. Indeed, simulation results demonstrated the potential of the Marangoni effect to enable a mass transport process that is significantly faster than in the case of pure molecular diffusion. Simulating the two cases distinctly, the comparison was carried out by evaluating the relationship between the respective molar fluxes under steady-state conditions. Our results revealed that the Marangoni effect may increase mass transport capabilities, significantly exceeding pure diffusive flux by more than three orders of magnitude. Furthermore, we explored potential self-similar solutions characterizing the Marangoni phenomenon. Notably, a semi-empirical, dimensionless fitting equation able to predict the augmented mass transport as the Marangoni number varies was obtained and proposed. Finally, the complete salt-discharge process was studied. Results revealed a rapid decrease in salt concentration in the control volume, reaching seawater salinity levels in less than two hours. This time scale, which is less than the overnight time of natural inactivity for solar distillation devices, ensures stable performance over time.

Understanding the impact of the Marangoni effect on salt rejection is crucial for leveraging and engineering this phenomenon effectively. Precise evaluation of rejection times enables optimization of system design and operational parameters, enhancing energy efficiency and cost-effectiveness of desalination devices. In perspective, it would be interesting to integrate the Navier–Stokes equations and the transport of diluted species with the energy balance equation, thus exploring the potential impact of any thermophoresis effects, and to explore the effect of the porosity of the structured capillary layer evaporator on the salt rejection performance. Moreover, shorter salt-rejecting times are particularly vital for prompt access to clean water in disaster areas, enabling better resource planning, and reducing environmental impact.

## CRedit authorship contribution statement

**Giovanni Stincone:** Methodology, Software, Formal analysis, Investigation, Data curation, Writing – original draft, Visualization. **Roberto Raffaele Meo:** Formal analysis, Investigation, Writing – original draft, Visualization. **Eliodoro Chiavazzo:** Formal analysis, Writing – review & editing, Supervision. **Pietro Asinari:** Formal analysis, Writing – review & editing, Supervision. **Matteo Fasano:** Formal analysis, Resources, Funding acquisition, Writing – review & editing, Supervision. **Matteo Morciano:** Conceptualization, Methodology, Software, Formal analysis, Investigation, Data curation, Writing – original draft, Writing – review & editing, Visualization, Supervision.

## Declaration of competing interest

The authors declare that they have no known competing financial interests or personal relationships that could have appeared to influence the work reported in this paper.

## Data availability

Data will be made available on request.

## Acknowledgments

This work was funded by the European Union Horizon Europe Research and Innovation Programme under grant agreement number 101091915 (acronym “MEloDIZER”). Views and opinions expressed are however those of the author(s) only and do not necessarily reflect those of the European Union or the European Health and Digital Executive Agency (HADEA). Neither the European Union nor the granting authority can be held responsible for them. M.M., M.F. and E.C. thank the CleanWaterCenter@PoliTo.

## References

- [1] C.J. Vorosmarty, P. Green, J. Salisbury, R.B. Lammers, Global water resources: vulnerability from climate change and population growth, *science* 289 (5477) (2000) 284–288.
- [2] D. Molden, *Water for Food Water for Life: A Comprehensive Assessment of Water Management in Agriculture*, Routledge, 2013.
- [3] C.P. Kelley, S. Mohtadi, M.A. Cane, R. Seager, Y. Kushnir, Climate change in the fertile crescent and implications of the recent Syrian drought, *Proc. Natl. Acad. Sci.* 112 (11) (2015) 3241–3246.
- [4] M.M. Mekonnen, A.Y. Hoekstra, Four billion people facing severe water scarcity, *Sci. Adv.* 2 (2) (2016) e1500323.
- [5] M.S. Mauter, P.S. Fiske, Desalination for a circular water economy, *Energy Environ. Sci.* 13 (10) (2020) 3180–3184.
- [6] GDP per capita (current US\$), Retrieved November 11, 2020, from World Bank website, <https://data.worldbank.org/indicator/NY.GDP.PCAP.CD>.
- [7] P. De Angelis, M. Tuninetti, L. Bergamasco, L. Calianno, P. Asinari, F. Laio, M. Fasano, Data-driven appraisal of renewable energy potentials for sustainable freshwater production in africa, *Renew. Sust. Energ. Rev.* 149 (2021) 111414.
- [8] H. Ghasemi, G. Ni, A.M. Marconnet, J. Loomis, S. Yerci, N. Miljkovic, G. Chen, Solar steam generation by heat localization, *Nat. Commun.* 5 (1) (2014) 4449.
- [9] E. Chiavazzo, M. Morciano, F. Viglino, M. Fasano, P. Asinari, Passive solar high-yield seawater desalination by modular and low-cost distillation, *Nature sustainability* 1 (12) (2018) 763–772.
- [10] P. Tao, G. Ni, C. Song, W. Shang, J. Wu, J. Zhu, G. Chen, T. Deng, Solar-driven interfacial evaporation, *Nat. Energy* 3 (12) (2018) 1031–1041.
- [11] G. Ni, G. Li, S.V. Boriskina, H. Li, W. Yang, T. Zhang, G. Chen, Steam generation under one sun enabled by a floating structure with thermal concentration, *Nat. Energy* 1 (9) (2016) 1–7.
- [12] Y. Zhang, T. Xiong, D.K. Nandakumar, S.C. Tan, Structure architecting for salt-rejecting solar interfacial desalination to achieve high-performance evaporation with in situ energy generation, *Adv. Sci.* 7 (9) (2020) 1903478.
- [13] M. Sheng, Y. Yang, X. Bin, S. Zhao, C. Pan, F. Nawaz, W. Que, Recent advanced self-propelling salt-blocking technologies for passive solar-driven interfacial evaporation desalination systems, *Nano Energy* 89 (2021) 106468.
- [14] R.R. Meo, M. Morciano, Investigating the potentials and limitations of capillary-fed vapor generators: a heat and mass transfer study, *International Communications in Heat and Mass Transfer* 137 (2022) 106309.
- [15] L. Zhou, Y. Tan, D. Ji, B. Zhu, P. Zhang, J. Xu, Q. Gan, Z. Yu, J. Zhu, Self-assembly of highly efficient, broadband plasmonic absorbers for solar steam generation, *Sci. Adv.* 2 (4) (2016) e1501227.

- [16] M.S. Mauter, I. Zucker, F. Perreault, J.R. Werber, J.-H. Kim, M. Elimelech, The role of nanotechnology in tackling global water challenges, *Nature Sustainability* 1 (4) (2018) 166–175.
- [17] Y. Wang, C. Wang, X. Song, S.K. Megarajan, H. Jiang, A facile nanocomposite strategy to fabricate a rgo-mwcnt photothermal layer for efficient water evaporation, *J. Mater. Chem. A* 6 (3) (2018) 963–971.
- [18] Z. Wang, Y. Liu, P. Tao, Q. Shen, N. Yi, F. Zhang, Q. Liu, C. Song, D. Zhang, W. Shang, et al., Bio-inspired evaporation through plasmonic film of nanoparticles at the air–water interface, *Small* 10 (16) (2014) 3234–3239.
- [19] K. Bae, G. Kang, S.K. Cho, W. Park, K. Kim, W.J. Padilla, Flexible thin-film black gold membranes with ultrabroadband plasmonic nanofocusing for efficient solar vapour generation, *Nat. Commun.* 6 (1) (2015) 10103.
- [20] J. Wang, Y. Li, L. Deng, N. Wei, Y. Weng, S. Dong, D. Qi, J. Qiu, X. Chen, T. Wu, High-performance photothermal conversion of narrow-bandgap  $\text{TiO}_2$  nanoparticles, *Adv. Mater.* 29 (3) (2017) 1603730.
- [21] X. Li, W. Xu, M. Tang, L. Zhou, B. Zhu, S. Zhu, J. Zhu, Graphene oxide-based efficient and scalable solar desalination under one sun with a confined 2d water path, *Proc. Natl. Acad. Sci.* 113 (49) (2016) 13953–13958.
- [22] K.-K. Liu, Q. Jiang, S. Tadepalli, R. Raliya, P. Biswas, R.R. Naik, S. Singamaneni, Wood–graphene oxide composite for highly efficient solar steam generation and desalination, *ACS Appl. Mater. Interfaces* 9 (8) (2017) 7675–7681.
- [23] Y. Yang, R. Zhao, T. Zhang, K. Zhao, P. Xiao, Y. Ma, P.M. Ajayan, G. Shi, Y. Chen, Graphene-based standalone solar energy converter for water desalination and purification, *ACS Nano* 12 (1) (2018) 829–835.
- [24] Z. Li, Y. Xing, X. Fan, L. Lin, A. Meng, Q. Li, Rgo/protonated g-c3n4 hybrid membranes fabricated by photocatalytic reduction for the enhanced water desalination, *Desalination* 443 (2018) 130–136.
- [25] X. Huang, Y.-H. Yu, O.L. de Llergo, S.M. Marquez, Z. Cheng, Facile polypyrrole thin film coating on polypropylene membrane for efficient solar-driven interfacial water evaporation, *RSC Adv.* 7 (16) (2017) 9495–9499.
- [26] W. Li, Z. Li, K. Bertelsmann, D.E. Fan, Portable low-pressure solar steaming-collection unisystem with polypyrrole origamis, *Adv. Mater.* 31 (29) (2019) 1900720.
- [27] Y. Shi, R. Li, Y. Jin, S. Zhuo, L. Shi, J. Chang, S. Hong, K.-C. Ng, P. Wang, A 3d photothermal structure toward improved energy efficiency in solar steam generation, *Joule* 2 (6) (2018) 1171–1186.
- [28] Z. Lei, X. Sun, S. Zhu, K. Dong, X. Liu, L. Wang, X. Zhang, L. Qu, X. Zhang, Nature inspired mxene-decorated 3d honeycomb-fabric architectures toward efficient water desalination and salt harvesting, *Nano Lett.* 14 (1) (2014) 10, <https://doi.org/10.1007/s40820-021-00748-7>.
- [29] Z. Lei, X. Sun, S. Zhu, K. Dong, X. Liu, L. Wang, X. Zhang, L. Qu, X. Zhang, Nature inspired mxene-decorated 3d honeycomb-fabric architectures toward efficient water desalination and salt harvesting, *Nano Lett.* 14 (1) (2014) 10.
- [30] G. Antonetto, M. Morciano, M. Alberghini, G. Malgaroli, A. Ciocia, L. Bergamasco, F. Spertino, M. Fasano, Synergistic freshwater and electricity production using passive membrane distillation and waste heat recovered from camouflaged photovoltaic modules, *J. Clean. Prod.* 318 (2021) 128464.
- [31] M. Morciano, M. Fasano, L. Bergamasco, A. Albiero, M.L. Curzio, P. Asinari, E. Chiavazzo, Sustainable freshwater production using passive membrane distillation and waste heat recovery from portable generator sets, *Appl. Energy* 258 (2020) 114086.
- [32] X. Dong, L. Cao, Y. Si, B. Ding, H. Deng, Cellular structured cnts@ sio2 nanofibrous aerogels with vertically aligned vessels for salt-resistant solar desalination, *Adv. Mater.* 32 (34) (2020) 1908269.
- [33] X. Hu, W. Xu, L. Zhou, Y. Tan, Y. Wang, S. Zhu, J. Zhu, Tailoring graphene oxide-based aerogels for efficient solar steam generation under one sun, *Adv. Mater.* 29 (5) (2017) 1604031.
- [34] H. Liu, C. Chen, G. Chen, Y. Kuang, X. Zhao, J. Song, C. Jia, X. Xu, E. Hitz, H. Xie, et al., High-performance solar steam device with layered channels: artificial tree with a reversed design, *Adv. Energy Mater.* 8 (8) (2018) 1701616.
- [35] X. Dong, Y. Si, C. Chen, B. Ding, H. Deng, Reed leaves inspired silica nanofibrous aerogels with parallel-arranged vessels for salt-resistant solar desalination, *ACS Nano* 15 (7) (2021) 12256–12266.
- [36] C. Liu, K. Hong, X. Sun, A. Natan, P. Luan, Y. Yang, H. Zhu, An ‘antifouling’ porous loofah sponge with internal microchannels as solar absorbers and water pumps for thermal desalination, *J. Mater. Chem. A* 8 (25) (2020) 12323–12333.
- [37] Z. Guo, G. Wang, X. Ming, T. Mei, J. Wang, J. Li, J. Qian, X. Wang, Pegylated self-growth mos2 on a cotton cloth substrate for high-efficiency solar energy utilization, *ACS Appl. Mater. Interfaces* 10 (29) (2018) 24583–24589.
- [38] E. Chiavazzo, Critical aspects to enable viable solar-driven evaporative technologies for water treatment, *Nat. Commun.* 13 (1) (2022) 5813.
- [39] Y. Kuang, C. Chen, S. He, E.M. Hitz, Y. Wang, W. Gan, R. Mi, L. Hu, A high-performance self-regenerating solar evaporator for continuous water desalination, *Adv. Mater.* 31 (23) (2019) 1900498.
- [40] Y. Yang, X. Yang, L. Fu, M. Zou, A. Cao, Y. Du, Q. Yuan, C.-H. Yan, Two-dimensional flexible bilayer janus membrane for advanced photothermal water desalination, *ACS Energy Lett.* 3 (5) (2018) 1165–1171.
- [41] Q. Zhang, G. Yi, Z. Fu, H. Yu, S. Chen, X. Quan, Vertically aligned janus mxene-based aerogels for solar desalination with high efficiency and salt resistance, *ACS Nano* 13 (11) (2019) 13196–13207.
- [42] L. Zhang, X. Li, Y. Zhong, A. Leroy, Z. Xu, L. Zhao, E.N. Wang, Highly efficient and salt rejecting solar evaporation via a wick-free confined water layer, *Nat. Commun.* 13 (1) (2022) 849.
- [43] M. Zou, Y. Zhang, Z. Cai, C. Li, Z. Sun, C. Yu, Z. Dong, L. Wu, Y. Song, 3d printing a biomimetic bridge-arch solar evaporator for eliminating salt accumulation with desalination and agricultural applications, *Adv. Mater.* 33 (34) (2021) 2102443.
- [44] C.A. Quist-Jensen, A. Ali, S. Mondal, F. Macedonio, E. Drioli, A study of membrane distillation and crystallization for lithium recovery from high-concentrated aqueous solutions, *J. Membr. Sci.* 505 (2016) 167–173.
- [45] C.A. Quist-Jensen, F. Macedonio, D. Horbez, E. Drioli, Reclamation of sodium sulfate from industrial wastewater by using membrane distillation and membrane crystallization, *Desalination* 401 (2017) 112–119.
- [46] A.K. Menon, I. Haechler, S. Kaur, S. Lubner, R.S. Prasher, Enhanced solar evaporation using a photo-thermal umbrella for wastewater management, *Nature Sustainability* 3 (2) (2020) 144–151.
- [47] W. Wang, Y. Shi, C. Zhang, S. Hong, L. Shi, J. Chang, R. Li, Y. Jin, C. Ong, S. Zhuo, et al., Simultaneous production of fresh water and electricity via multistage solar photovoltaic membrane distillation, *Nat. Commun.* 10 (1) (2019) 3012.
- [48] Y. Shi, C. Zhang, R. Li, S. Zhuo, Y. Jin, L. Shi, S. Hong, J. Chang, C. Ong, P. Wang, Solar evaporator with controlled salt precipitation for zero liquid discharge desalination, *Environ. Sci. Technol.* 52 (20) (2018) 11822–11830.
- [49] G. Ni, S.H. Zandavi, S.M. Javid, S.V. Boriskina, T.A. Cooper, G. Chen, A salt-rejecting floating solar still for low-cost desalination, *Energy Environ. Sci.* 11 (6) (2018) 1510–1519.
- [50] V. Kashyap, A. Al-Bayati, S.M. Sajadi, P. Irajizad, S.H. Wang, H. Ghasemi, A flexible anti-clogging graphite film for scalable solar desalination by heat localization, *J. Mater. Chem. A* 5 (29) (2017) 15227–15234.
- [51] J. Xiao, Y. Guo, W. Luo, D. Wang, S. Zhong, Y. Yue, C. Han, R. Lv, J. Feng, J. Wang, et al., A scalable, cost-effective and salt-rejecting mos2/sa@ melamine foam for continuous solar steam generation, *Nano Energy* 87 (2021) 106213.
- [52] J. Gao, L. Zhang, J. You, Z. Ye, Y. Zhong, R. Wang, E.N. Wang, Z. Xu, Extreme salt-resisting multistage solar distillation with thermohaline convection, *Joule* 7 (10) (2023) 2274–2290.
- [53] M. Morciano, M. Fasano, S.V. Boriskina, E. Chiavazzo, P. Asinari, Solar passive distiller with high productivity and marangoni effect-driven salt rejection, *Energy Environ. Sci.* 13 (10) (2020) 3646–3655.
- [54] Y. Chen, J. Yang, L. Zhu, S. Wang, X. Jia, Y. Li, D. Shao, L. Feng, H. Song, Marangoni-driven biomimetic salt secretion evaporator, *Desalination* 548 (2023) 116287.
- [55] S. Luo, Z. Li, X. Cui, Y. Ge, An anti-salt accumulation 2.5 d arch solar-driven evaporator based on marangoni effect for seawater desalination, *Chem. Eng. J.* 454 (2023) 140286.
- [56] Q. Huang, C. Du, C. Guo, C. Huang, X. Wang, A high-efficiency salt-rejecting solar evaporator with optimized porous structure for continuous solar desalination, *Appl. Therm. Eng.* 187 (2021) 116515.
- [57] L. Wu, Z. Dong, Z. Cai, T. Ganapathy, N.X. Fang, C. Li, C. Yu, Y. Zhang, Y. Song, Highly efficient three-dimensional solar evaporator for high salinity desalination by localized crystallization, *Nat. Commun.* 11 (1) (2020) 521.
- [58] M. Alberghini, M. Morciano, M. Giordano, F. Perrucci, L. Scaltrito, D. Janner, E. Chiavazzo, M. Fasano, P. Asinari, Textured and rigid capillary materials for passive energy-conversion devices, *Adv. Mater. Interfaces* 9 (18) (2022) 2200057.
- [59] Y. Chen, S. Yang, Z. Wang, M. Elimelech, Transforming membrane distillation to a membraneless fabric distillation for desalination, *Nature Water* (2024) 1–10.
- [60] R. Ranjan, J.Y. Murthy, S.V. Garimella, A microscale model for thin-film evaporation in capillary wick structures, *Int. J. Heat Mass Transf.* 54 (1–3) (2011) 169–179.
- [61] N. Deka, S. Dash, Multistage interfacial thermal desalination system with metallic evaporators, *Desalination* 556 (2023) 116576.
- [62] L. Wang, L.P. Wang, Z. Guo, J. Mi, Volume-averaged macroscopic equation for fluid flow in moving porous media, *Int. J. Heat Mass Transf.* 82 (2015) 357–368.
- [63] Y. Habtemichael, R. Kiflemariam, H. Fuentes, Evaluation of instability of a low-salinity density-dependent flow in a porous medium, in: COMSOL Conference, Boston, COMSOL, Inc, Burlington, MA, 2014.
- [64] M.C. Boufadel, A mechanistic study of nonlinear solute transport in a groundwater–surface water system under steady state and transient hydraulic conditions, *Water Resour. Res.* 36 (9) (2000) 2549–2565.
- [65] V. Vitagliano, P.A. Lyons, Diffusion coefficients for aqueous solutions of sodium chloride and barium chloride, *J. Am. Chem. Soc.* 78 (8) (1956) 1549–1552.
- [66] R.R. Meo, M. Provenzano, M. Morciano, Investigating the solute concentration in capillary-fed vapor generators: a heat and mass transfer study, *International Communications in Heat and Mass Transfer* 148 (2023) 106998.
- [67] D. Boniface, C. Cottin-Bizonne, F. Detchewerry, C. Ybert, Role of marangoni forces in the velocity of symmetric interfacial swimmers, *Physical Review Fluids* 6 (10) (2021) 104006.